Nanoscale Advances

PAPER

View Article Online
View Journal | View Issue

Cite this: *Nanoscale Adv.*, 2019, **1**, 4481

Surface-passivated, soluble and non-toxic graphene nano-sheets for the selective sensing of toxic Cr(VI) and Hg(II) metal ions and as a blue fluorescent ink

Ruchi Aggarwal,[a] Satyesh Raj Anand,[a] Deepika Saini,[a] Gunture,[a] Ravindra Singh,[b] Amit Kumar Sonker*[c] and Sumit Kumar Sonkar*[a]

Received 15th June 2019
Accepted 2nd October 2019

DOI: 10.1039/c9na00377k

rsc.li/nanoscale-advances

Non-toxic amine-functionalized soluble graphene nano-sheets (f-GNS) were synthesized by using an old and well-known simple organic procedure. The f-GNS exhibited enhanced optical properties, such as strong blue fluorescence emission with a high value of quantum yield (~13%). The O,O′-bis-(2-aminopropyl) polypropylene glycol-*block*-polyethylene glycol-*block*-polypropylene glycol 800 as block polymeric amine (BPA)-passivized surface of f-GNS exhibited high aqueous solubility and excitation-dependent fluorescence emission behavior with a strong photo-stability performance. These f-GNS were tested for the significant selective sensing of toxic metal ions Cr(VI) and Hg(II) from various tested toxic metal ions. The sensing experiment was supported by cyclic voltammetry analysis. The dual metal ion sensing method based on fluorescence showed the limit of detection (LOD) of ~56 nM for Cr(VI) and ~45 nM for Hg(II) through a fluorescence quenching process. f-GNS were found to be non-toxic when tested over *Escherichia coli* (*E.coli*) cells. Additionally, the strong blue emission properties of f-GNS enabled their use as a suitable blue fluorescent ink under UV light illumination.

1. Introduction

The surface passivation and surface functionalization of nano-carbons *via* structural[1,2] and chemical[3] methods has enabled researchers to solubilize them. As compared to raw nano-carbons having weak fluorescence optical properties, surface-passivated[4] aqueous-solubilized nano-carbons shows improved optical properties. Generally, the functionalized versions of nano-carbons are full of surface defects[2,3] formed by long-known method of oxidation, which originates from refluxing of the insoluble nano-carbons with acids like nitric acid (HNO_3)[5] or a mixture of nitric acid and sulphuric acid (HNO_3 + H_2SO_4).[6] Surface oxidation introduces a significant number of negative surface functional groups,[6,7] such as alcohol (–OH), carboxyl (–COOH), and ketones (–COR), on the surface of the nano-carbons. Furthermore, the fluorescence optical properties of these nanocarbons can be improved by modifying the negatively charged surface groups using organic amine moieties (such as oligomeric polyethylene glycol diamine (PEG_{1500N}), amino polymer (PPEI-EI),[8] octadecylamine,[8] ethanolamine,[8] and polydopamine, 2,2′-(ethylenedioxy)bis(ethylamine)). Similar to the observation for other forms of nano-carbons, the solubility of multilayered graphene nano-sheets (GNS) can be easily achieved by their functionalization. Over the last years, a series of methods have been developed for the direct functionalization of GNS, such as amidation,[9] aryne cycloaddition,[10] 1,3-dipolar cycloaddition,[11] diazonium coupling,[12] and nitrene addition.[13] Out of many documented processes, the amidation of graphene with polymeric amines can significantly enhance its solubility in aqueous media, which can be related to its vast future applicability in biological sciences. For example, Berry *et al.* synthesized a new graphene-derived live-bacterial-hybrid device and a DNA-hybridized device with excellent sensitivity.[14] Dai *et al.* formed nanoscale sheets of graphene oxide (GO) using branched polyethylene glycol (PEG) and showed the unique ability of graphene during the attachment and delivery of aromatic insoluble drugs.[15] Li and Wallace *et al.* presented the growth of mouse fibroblast cells (L-929) on a graphene paper, which indicated the biocompatibility of graphene paper and been suitable for biomedical applications.[16] Fan *et al.* reported that the oxide of graphene facilitated electron transfer for a metalloprotein at the surface of electrode.[17]

Over the past years, in addition to the already explained applications of GNS, several fluorescence-based sensing probes

[a]*Department of Chemistry, Malaviya National Institute of Technology, Jaipur-302017, India. E-mail: sksonkar.chy@mnit.ac.in*

[b]*Department of Chemistry, Maharani Shri Jaya Government Post-Graduate College, Bharatpur, Rajasthan-321001, India*

[c]*Department of Materials Science and Engineering, Department of Bio-nanotechnology Gachon University, Gyeonggi-do, South Korea. E-mail: amitsonker28@gmail.com*

have been developed for the detection of metal ions, particularly toxic metal ions such as Cr(VI) and Hg(II). For example, Cr(VI) is a well-known toxic non-biodegradable pollutant[18] found in the effluent of many industrial processes, such as paint making, electroplating, and leather tanning;[19] and discarded[19,20] as wastewater, which is continuously harming the aquatic systems and causing devastating consequences.[19,21] Mercury Hg(II) is observed in many chemical forms such as organic (dimethylmercury, phenylmercury) and inorganic salts (Hg(I) and Hg(II)) and the elemental form. It is a highly toxic metal element responsible for serious health problems that affect the kidney[22] and cause neurological dysfunctions such as the Minamata disease and central nervous system (CNS) failure.[23] The permissible limits for Cr(VI) and Hg(II) are 50 μg L^{-1},[24] and 2 ng mL^{-1},[25] respectively, according to the World Health Organization (WHO). Considering all these parameters, there is a need for effective sensors for the selective sensing of these metal ions below the permissible limit.

The present study deals with the water-soluble versions of functionalized graphene nano-sheets (f-GNS), were prepared *via* a simple functionalization method and explored them for the selective sensing of the metal ions Cr(VI) and Hg(II) based on a fluorescence method. The surface passivation of graphene using *O*,*O*′-bis-(2-aminopropyl) polypropylene glycol-*block*-polyethylene glycol-*block*-polypropylene glycol 800 as the block polymeric amine (BPA) facilitated multi-emissive fluorescence properties in f-GNS. The BPA-functionalized f-GNS possessed numerous fluorescence active sites, which upon interaction with Cr(VI) and Hg(II) significantly quenched the fluorescence of f-GNS. To explore the future biological applications of f-GNS, their non-toxicity was examined on *Escherichia coli* (*E. coli*) cells up to the limit of 15 mg mL^{-1}. The initial results were in favor of f-GNS, which showed that up to the tested limit, f-GNS were non-toxic. Another application of f-GNS was also presented as they could be used as a blue fluorescent ink and thus be used for stamping and writing purposes.

2. Experimental section

2.1 Materials

All the selected metal salts and chemical reagents used in the present study were of analytical grade and used directly. Lead nitrate [$Pb(NO_3)_2$], cupric nitrate [$Cu(NO_3)_2$], barium nitrate [$Ba(NO_3)_2$], mercuric bromide ($HgBr_2$), aluminum nitrate [$Al(NO_3)_3$], bismuth nitrate [$Bi(NO_3)_3 \cdot 5H_2O$], cobalt nitrate [$Co(NO_3)_2$], strontium nitrate [$Sr(NO_3)_2$], nickel nitrate [$Ni(NO_3)_2 \cdot 6H_2O$], cadmium nitrate [$Cd(NO_3)_2 \cdot H_2O$], GNS, thionyl chloride ($SOCl_2$), tetra-*n*-butyl ammonium bromide (TBAB), deuterium oxide (D_2O) and BPA were purchased from Sigma Aldrich, India, and the graphene samples were obtained from Tata Steel Limited.

2.2 Synthesis of f-GNS

The oxidation of GNS (200 mg) was performed by refluxing it using a 3 : 1 mixture of nitric acid (HNO_3)[5] and DI water. The mixture was cooled down to room temperature and centrifuged at 5000 rpm to collect the black residue. The obtained black residue was repeatedly washed several times using distilled water to remove impurities and later dried at ~60 °C for 10 hours. In the next step, o-GNS (100 mg) was added to 5–6 mL $SOCl_2$ in a two-necked round bottom flask. The mixture was refluxed at ~80 °C for 4–5 hours and dried to obtain acyl chloride-modified GNS. After that, 1000 mg BPA was added to the same reaction mixture, heated at ~180 °C under nitrogen protection for ~6 hours and cooled down to room temperature to obtain a red-brown color solution. Later, the mixture was centrifuged at 8000 rpm for 15 min to obtain non-toxic soluble graphene nano-sheets (f-GNS).

2.3 Cyclic voltammetry setup

The electrochemical sensing of Cr(VI) and Hg(II) metal ions by f-GNS was performed using a three electrode system. The setup contained a Pt electrode as the working electrode, a Pt wire as an auxiliary electrode, and Ag/AgCl as the reference electrode. For electrochemical response, 1 μL mL^{-1} stock solution of f-GNS was prepared. Also, 0.1 M TBAB solution was used as the supporting electrolyte, and the scan rate was fixed at 50 mV s^{-1}.

2.4. Toxicity assessment of f-GNS

In this assay, an overnight grown culture of *E. coli* was inoculated in freshly prepared Luria Bertani (LB) broth and was placed in a shaker incubator, which was stirred at 150 rpm for 1–2 h at 35 °C (±1 °C) so as to achieve final OD_{600} (optical density at 600 nm) of 0.5 (±0.05). For the evaluation of toxicity, 100 μL *E. coli* culture was added to autoclaved 3 mL LB broth tubes, and 100 μL of f-GNS at three different concentrations (5 mg mL^{-1}, 10 mg mL^{-1} and 15 mg mL^{-1}) was added separately in different tubes. This test was conducted with reference to one blank (3.1 mL LB + 100 μL distilled water) and three different concentrations. These are control (3 mL LB + 100 μL *E. coli* culture + 100 μL distilled water) and (3.1 mL LB + 100 μL *E. coli* culture + 100 μL f-GNS). All the prepared tubes in three replicates were placed in a shaker incubator, which was stirred at 100 rpm for 18 h at 35 °C (±1 °C), following which the optical density of each tube was measured at 600 nm.

2.5 Quantum yield (QY) measurements

The QY of f-GNS was measured by using quinine sulphate as the reference dye (QY = 54% at excitation wavelength 348 nm) using the following equation:

$$QY = QY_{ref} \times \frac{I}{I_{ref}} \times \frac{A_{ref}}{A} \times \frac{\eta^2}{\eta_{ref}{}^2}$$

here, QY is the quantum yield, I is the integrated fluorescence emission intensity, η is the refractive index of the solvent, and A is the absorbance. The term ref represents the reference dye (quinine sulphate).[27,28] The solution of quinine sulphate was made by dissolving it in 0.5 M H_2SO_4. The same excitation wavelength was applied for the f-GNS aqueous solution.

2.6 Characterization

The morphological characterization of f-GNS was performed using transmission electron microscopy (TEM) and high resolution transmission electron microscopy (HRTEM) using model Tecnai 20 G2 with an accelerating voltage of 300 kV. UV-vis absorption spectral analysis was performed at room temperature with a Jasco V-730 spectrophotometer. Fluorescence spectral analysis was performed in aqueous solutions at room temperature with a Fluoromax 4C.L. spectrophotometer. The atomic force microscopy (AFM) image analysis of f-GNS was conducted on Pico SPM (Molecular Imaging) to study its surface topology. Fourier transform infrared (FTIR) spectra were obtained using KBr pellets with a Bruker Vertex 70 FT-IR spectrophotometer. Cyclic voltammetry (CV) experiments were performed on the setup K-Lyte 1.2 model from Kanopy Techno Solutions Pvt. Ltd. Bacterial applications were carried out using a UV-1800 SHIMADZU spectrophotometer. ^{1}H-NMR (Nuclear Magnetic Resonance) analysis was carried out on JEOL ECS 400 (operating at 400 MHz) using D_2O as the solvent.

3. Results and discussion

The simple approach of functionalization used in this study is shown as a schematic diagram in Scheme 1. GNS were oxidized using HNO_3 to achieve the oxidized version of GNS (denoted as o-GNS), which on further reaction with thionyl chloride (in a nitrogen environment) formed acylated-GNS containing –COCl moieties. In the final step, these acylated-GNS were reacted with BPA under the protection of a nitrogen environment to acquire BPA-functionalized water-soluble GNS denoted as f-GNS. These f-GNS showed fluorescence-based selective sensing towards the toxic metal ions, namely, Cr(VI) and Hg(II) based on the simple mechanism of fluorescence quenching. These f-GNS were found to be biocompatible when tested over *E. coli* cells. Additionally, these were further explored as a blue-emitting fluorescent ink when illuminated under a UV light.

3.1 Microscopic analysis

Transmission electron microscopy (TEM) was used for the morphological and microstructural analyses of f-GNS. Fig. 1(a and b) show the low-resolution TEM images of f-GNS, indicating the presence of layered f-GNS overlapping with each other. The high-resolution TEM (HRTEM) image of f-GNS displayed in Fig. 1(c) shows the presence of multiple layers in f-GNS. The HRTEM image shown in Fig. 1(d) is the magnified portion of Fig. 1(c) (blue box), indicating the graphitic interlayer spacing (*d* spacing), which was found to be 0.36 nm. Fig. 1(e) shows the topographical AFM image of f-GNS, and Fig. 1(f) represents its corresponding height profile analysis.

3.2 Spectroscopic analysis

FTIR and NMR. The surface functionalization of f-GNS *via* BPA molecules was investigated by a comparative analysis of the FTIR and ^{1}H-NMR spectra. Fig. 2(a) shows the comparison of the FTIR spectra of BPA (black line), o-GNS (red line) and f-GNS (blue line). A comparable broad peak was observed at

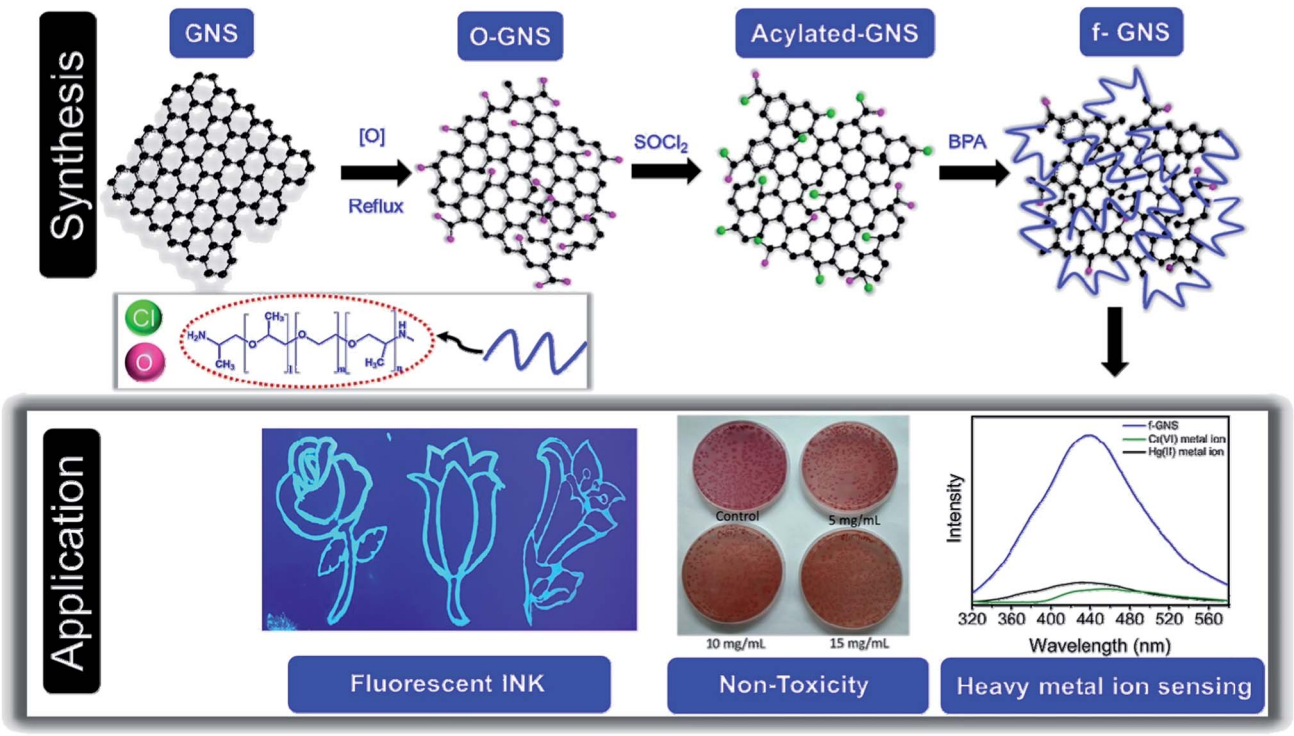

Scheme 1 Schematic representation showing the synthesis of f-GNS. f-GNS were used for the sensing of toxic metal ions Cr(VI) and Hg(II) based on fluorescence quenching. They also showed a non-toxic behavior and were used as a blue fluorescent ink.

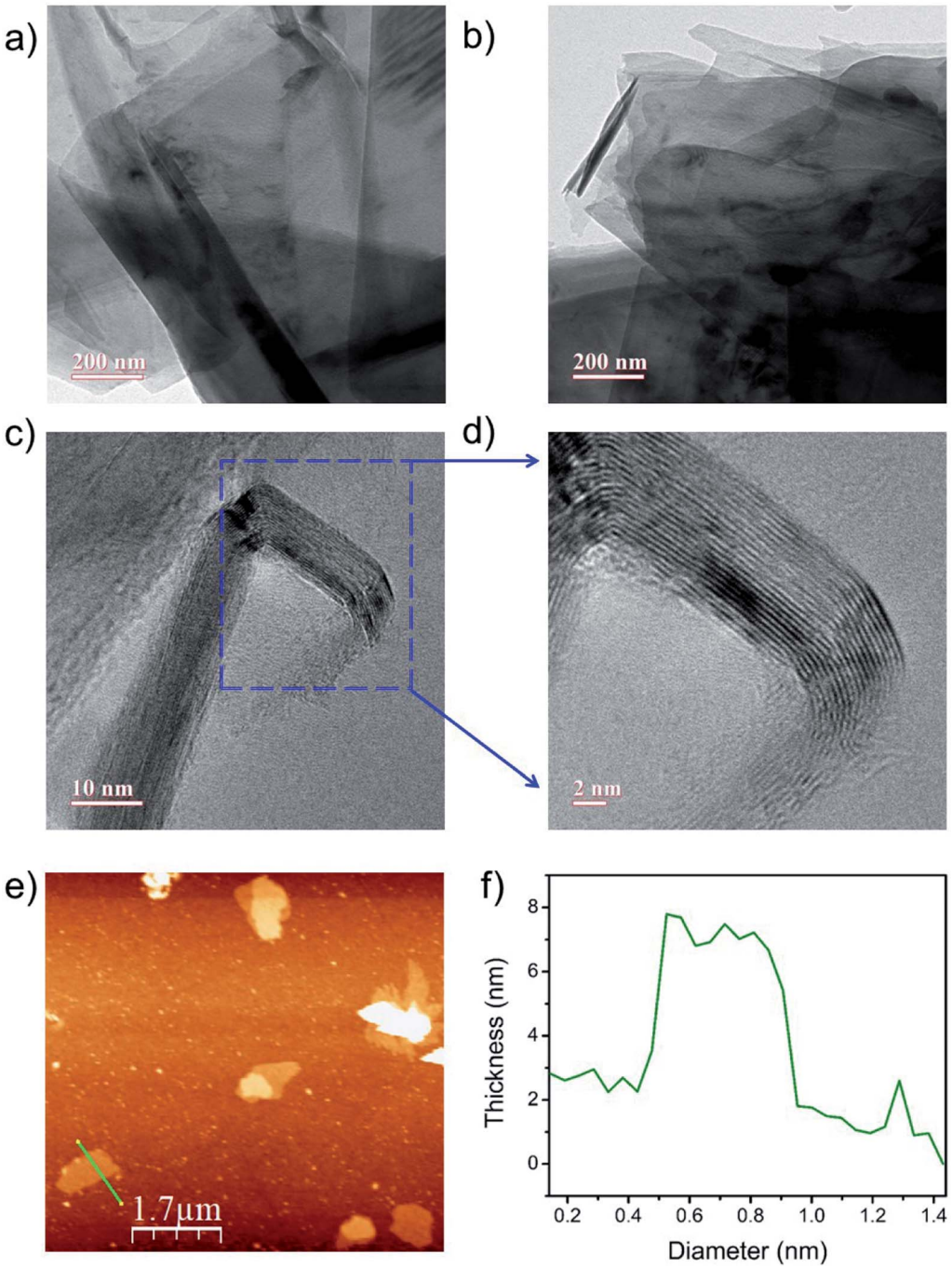

Fig. 1 (a and b) Low-resolution TEM micrographs of f-GNS; (c) HRTEM image of f-GNS; (d) magnified image of the fringes (blue box in (c)); (e) AFM image of f-GNS and (f) its corresponding height profile diagram.

$\sim$3460 cm^{-1} in the f-GNS spectrum, corresponding to the merging of the –OH/–NH bonds[29,30] present in BPA and o-GNS. The increased intensity of the C–H stretching band at $\sim$2860 cm^{-1} for f-GNS clearly indicated the bonding of the BPA molecules with o-GNS. Various stretching and bending vibrations of new polar groups (such as C=C, C=N, C=O, and C–O)[26,28] were observed in the merged region of $\sim$1600–600 cm^{-1} in the f-GNS spectra, supporting the functionalization process. A comparative NMR analysis (Fig. 2(b–d)) was conducted to confirm the surface functionalization of f-GNS by the BPA molecules. The chemical structure of BPA is displayed in Fig. 2(b), with the chemically different protons labelled. The number of repetitive units in each BPA molecule was given by $l + n = 6$ and $m = 39$. The BPA chain was attached by ether linkage, and the $-NH_2$ groups were only present at the terminal ends. In Fig. 2(c), the ^{1}H-NMR region from 3.8 to 2.6 ppm is represented along with a magnified image of the region from 3.6 to 2.9 ppm. Protons represented by g and g′ in BPA

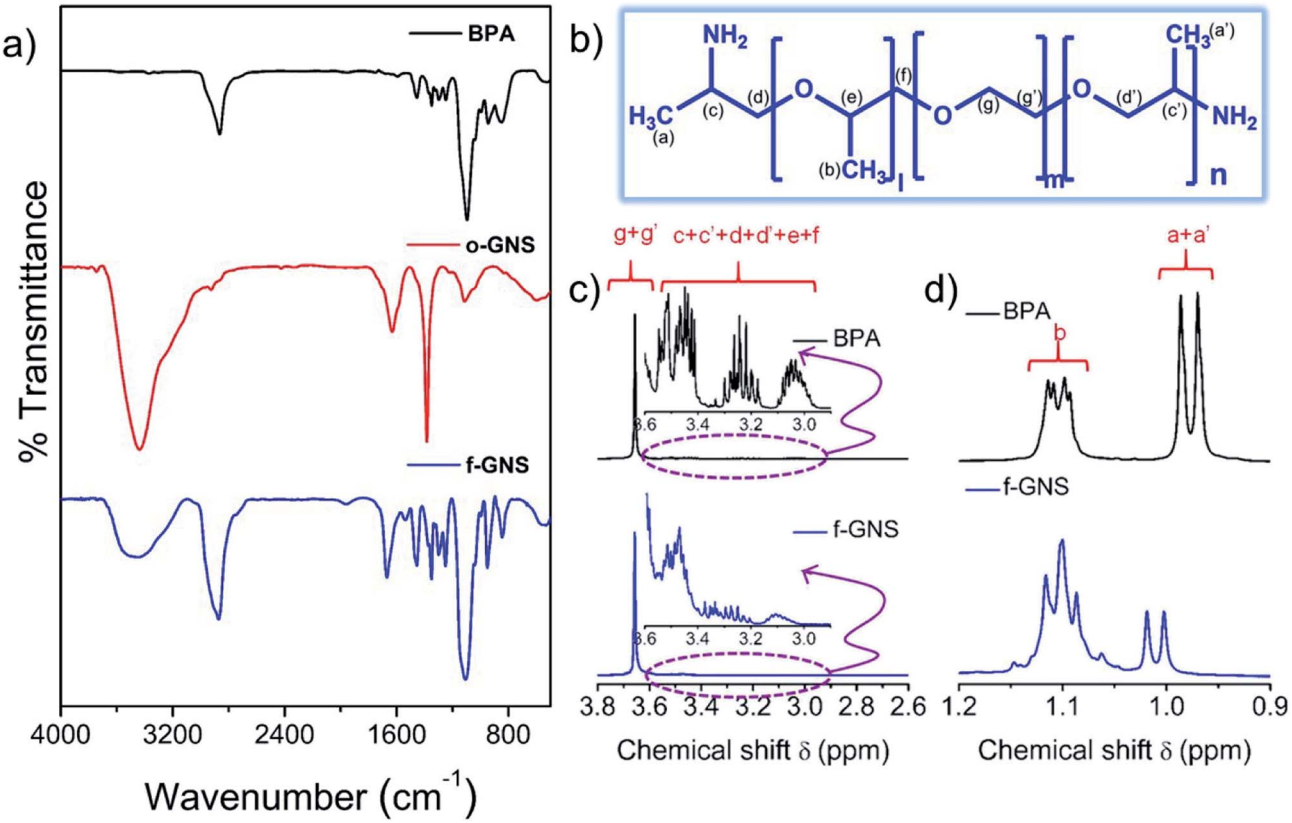

Fig. 2 (a) Comparative FT-IR spectra of BPA, o-GNS, and f-GNS; (b) the chemical structure of BPA; (c) comparative ^{1}H-NMR analysis of f-GNS with BPA along with the magnified image of the region from 3.6 to 2.9 ppm; (d) ^{1}H-NMR analysis of f-GNS with BPA in the region from 1.2 to 0.9 ppm.

belonged to unit $m = 39$ and were relatively more in number as compared to that for the other repeating units, which appeared as a broad signal after the functionalization of f-GNS. In the magnified spectra, the protons labelled as c, c′, d, d′, e and f are described, which shows the merging of different peaks of protons in f-GNS as compared to that for the BPA molecules. In Fig. 2(d), the region from 1.2 to 0.9 ppm depicts the region of the methylated protons present in close affinity to nitrogen groups and can have a direct influence over the formation of amide linkage. The protons labelled as a, a′ and b in BPA show a slight downfield shift and broadening[31] in the spectrum of f-GNS, which is perhaps due to the decreased mobility[32] of the BPA molecules.

3.3 UV-vis and fluorescence analyses

The optical properties of f-GNS were investigated by UV-vis spectroscopy. Fig. 3(a) shows the full UV-vis absorption spectra of f-GNS. The absorption spectra of f-GNS showed characteristic absorption peaks at ~215 nm and ~272 nm, corresponding to the π → π* and n-π* transition respectively,[2,28,33,34] which may be attributed to the presence of the C=C and C=O or C=N bonds associated with the BPA functionalization on the surface of f-GNS. The digital photographic images of f-GNS under normal daylight (left) and UV light (right) illumination are shown in Fig. 3(b). The emission properties of f-GNS were studied by varying the excitation wavelengths from 300 to 500 nm with the interval of 20 nm, as displayed in Fig. 3(c). The maximum emission was observed at the excitation wavelength of 380 nm in the blue fluorescent region. The QY of f-GNS was found to be ~13%. Fig. 3(d) displays the excellent photostability of f-GNS in a photobleaching experiment performed for 2 hours under continuous irradiation at 380 nm excitation.

3.4 Selective sensing properties of Cr(VI) and Hg(II)

The method of fluorescence quenching was used for the selective sensing of toxic metal ions by f-GNS, as described in Fig. 4(a). The fluorescence emission of f-GNS centered at 433 nm was used for the selective sensing[35] of various toxic metal ions which includes Pb(II), Cu(II), Ba(II), Hg(II), Cr(VI), Al(III), Bi(III), Sr(II), Ni(II) and Cd(II) by f-GNS. Among the tested toxic metal ions, f-GNS showed selectivity towards Cr(VI)[36] and Hg(II)[23] *via* the formation of f-GNS-Cr(VI)[36] and f-GNS-Hg(II)[23,37] complexes, respectively. Hence, a fluorescence-based relative change in the intensity of fluorescence using $(I_o–I)/I_o$ is displayed in Fig. 4(b), where I_o and I are the intensities of f-GNS without and with metal ions, respectively.

The fluorescence sensing[38] by f-GNS was investigated in the presence of the Cr(VI)[38,39] and Hg(II)[40] ions in aqueous media at their maximum emission (~433 nm). Fig. 4(c and f) show the

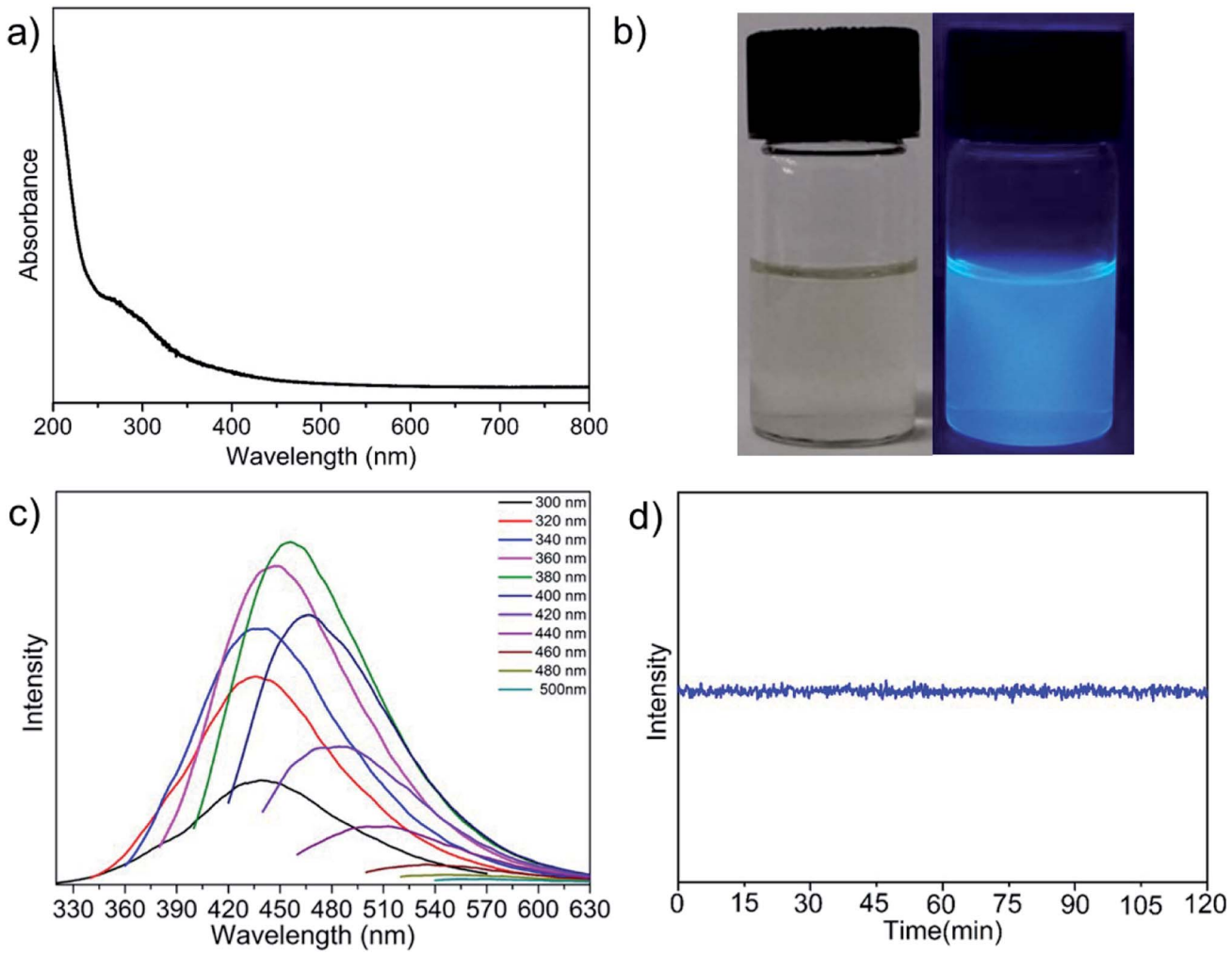

Fig. 3 (a) UV-vis absorption spectra of f-GNS; (b) digital photographic images of f-GNS irradiated under daylight (left) and UV light (right); (c) excitation-dependent fluorescence emission spectra of f-GNS (excited from 300 nm to 500 nm with an increment of 20 nm towards the red region); (d) photostability of f-GNS for 2 hours under continuous irradiation of 380 nm fluorescence excitation wavelength.

quenching effect of the gradual increase in the concentrations of Cr(VI) and Hg(II) ions on the fluorescence intensity of f-GNS. Quenching was observed in the range from 0 to 400 μM for Cr(VI) and from 0 to 571 μM for Hg(II). Fig. 4(d and g) show the decrease in the fluorescence intensity of f-GNS, depicting their quenching efficiency on increasing the concentration (in nM) of the toxic metal ions Cr(VI) and Hg(II). The fluorescence sensing of the toxic Cr(VI) and Hg(II) metal ions by f-GNS could be quantitatively determined using the Stern–Volmer equation:

$$\frac{I_o}{I} = 1 + K_{sv}[\mathrm{Cr(VI)\ \ or\ \ Hg(II)}]$$

here, I_o and I are the fluorescence intensities of f-GNS without and with the metal ions, respectively, [Cr(VI) or Hg(II)] is the concentration of the respective metal ion, and K_{sv} is the static Stern–Volmer[28] quencher constant. Fig. 4(e and h) show the graph of the relative change in fluorescence intensity I_o/I against the concentration of the metal ions Cr(VI) and Hg(II), respectively. As shown in Fig. 4(e), a linear relationship is observed in the range from 0 to 413 nM concentration of Cr(VI) with regression coefficient (R^2) of 0.98 and K_{sv} of 0.00104 nM^{-1}. In Fig. 4(h), a linear relationship is shown by Hg(II) in the concentration range from 0 to 74 nM with R^2 of 0.96 and a K_{sv} value of 0.00129 nM^{-1}. The lower limits of detection were calculated to be ~56 nM and ~45 nM for the toxic Cr(VI) and Hg(II) metal ions, respectively. A comparative analysis based on previous studies for the selective sensing of the toxic Cr(VI) and Hg(II) metal ions using different types of carbon nanoforms is given in Table 1 including the method reported here.

3.5 Cyclic voltammetry studies

The selective sensing ability of f-GNS towards the toxic Cr(VI) and Hg(II) metal ions was supported by cyclic voltammetry,[52,53] and the results are depicted in Fig. 5. In an aqueous solution, f-GNS displayed irreversible[54,55] redox responses at E_{oxi} = −0.76 V with +1.60 mA peak current *vs.* Ag/AgCl and E_{red} = +0.47 V with −0.06 mA peak current *vs.* Ag/AgCl. The redox

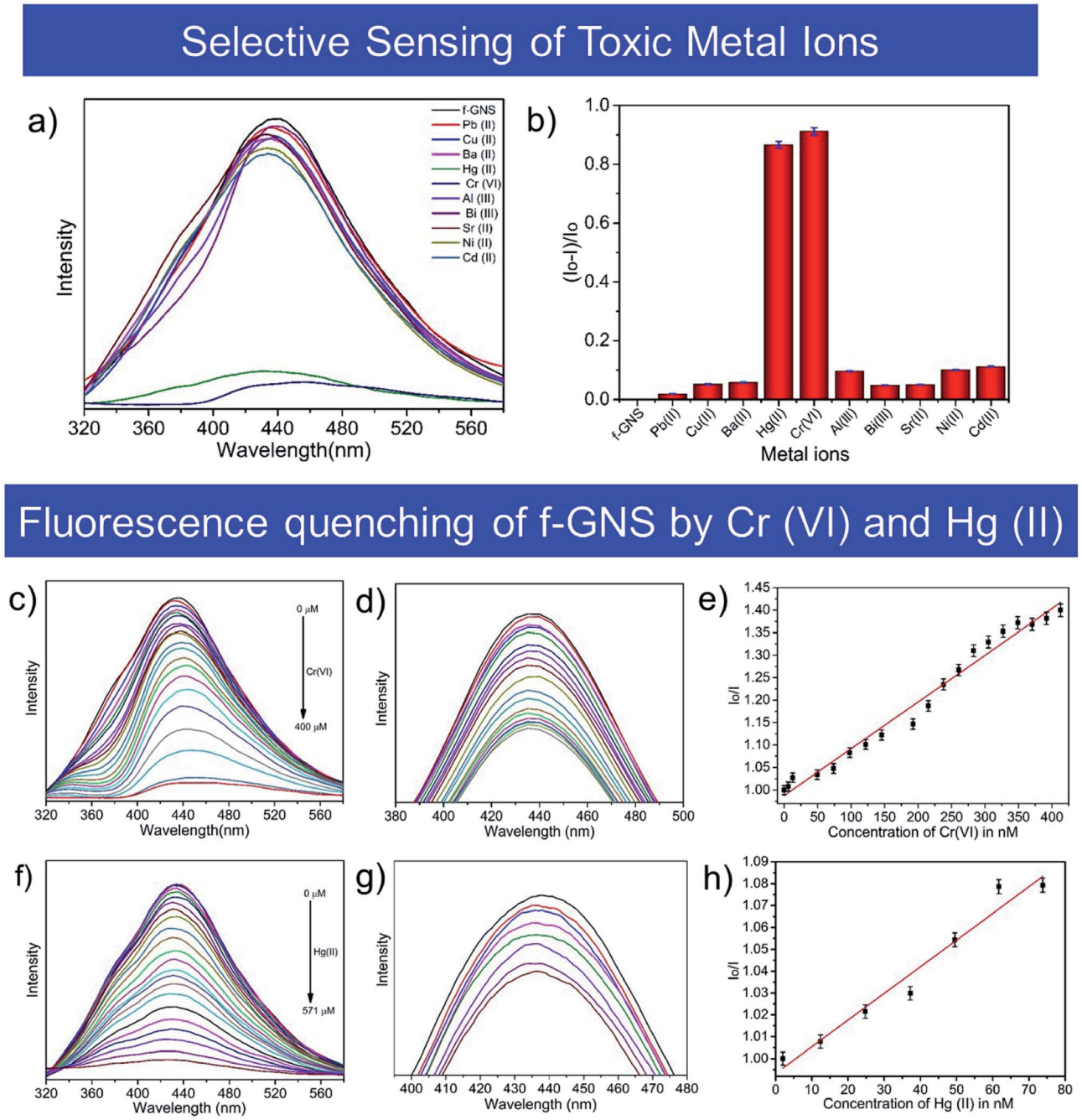

Fig. 4 (a) Fluorescence spectra showing the selective sensing of toxic metal ions by f-GNS; (b) relative changes in the fluorescence intensity of f-GNS in the presence of different metal ions; (c and f) fluorescence quenching spectra of f-GNS upon the addition of toxic Cr(VI) and Hg(II) ions at increasing concentrations; (d and g) fluorescence quenching on increasing the concentration of the metal ions (in nM); (e and h) Stern–Volmer plots of f-GNS fluorescence quenching by the addition of toxic Cr(VI) and Hg(II) ions.

responses for the addition of the two different metal ions Cr(VI) and Hg(II) at different concentrations were monitored using the electrochemical sensing system in the aqueous phase. After the addition of a 100 μM aqueous solution of Cr(VI) or Hg(II), one additional irreversible reductive redox response was generated at $E_{1/2} = -0.60$ V *vs.* Ag/AgCl in the case of Cr(VI) and $E_{1/2} = 0.02$ V *vs.* Ag/AgCl in the case of Hg(II). The redox peak intensity increased on increasing the concentration of the heavy metal ions from 100 μM to 200 μM (shown in Fig. 5(a and b)), resulting in the sensing of the toxic Cr(VI) and Hg(II) metal ions.

3.6 Possible mechanism for selective sensing

The possible mechanism for the selective sensing of the toxic metal ions by f-GNS has been described in Fig. 6. The fluorescence quenching by the metal ions could be explained based on

Table 1 Comparative table showing the ability of different nano-carbons in sensing Cr(VI) and Hg(II)

Source	Method synthesis/time	Excitation (nm)	Emission (nm)	LOD	Sensing	Type of material	Reference
Citric acid (CA)/NaOH	Heated, 200 °C, 30 min	365	450	0.439 nM	Hg(II)	GQDs	40
GO/acetonitrile/K_2CO_3/thymine	Heated, 60 °C, 1 h	340	448	400 ppb	Hg(II)	GO	41
H_2SO_4/H_3PO_4/$KMnO_4$/graphite powder	Stirred, 12 h	490	522	0.17 nM	Hg(II)	GO	42
GO/DMF/BODIPY 1	Heat	480	510	NA	Hg(II)	BGO	43
GO solution/$[Ru(bpy)_2(pip)]^2$	Sonicated at 20 °C for 20 minutes	455	605	2.34 nM	Hg(II)	GO-Ru hybrid	44
Petrol soot	Soxhlet	580	680	0.51 μM	Cr(VI)	wsGNS	3
Diethylenetriamine pentaacetic acid DTPA	Calcination, 400 °C, 20 min	370	420	0.15 μM	Cr(VI)	N-CNPs	45
Aspartic acid/diethylenetriamine/ phosphoric acid	Hydrothermal, 280 °C	340	410	0.48 μM	Cr(VI)	N,PCQDs	46
Pyrene/1,3,6-trinitropyrene/ammonia/ hydrazine hydrate	Hydrothermal, 200 °C, 8 h	420	496	190 nM	Cr(VI)	GQD	47
Glucose/H_2SO_4/EDA/	Carbonization	372	465	0.56 nM	Cr(VI)	S,N-CDs	48
Algal biomass	Hydrothermal, 200 °C, 3 h	340	415	0.018 μM	Hg(II) and Cr(VI)	NPCDs	49
Melamine/HNO_3	Refluxed, 120 °C, 24 h	310	438	0.15 μM	Cr(VI)	g-C_3N_4	38
EDTA·2Na/thiourea	Heat, 150–250 °C	360	433	0.01 nM	Hg(II)	SCNQDs	50
Corn bract/anhydrous ethanol/H_2N-PEG-NH_2/Na_2CO_3	Heated to 100 °C, 24 h	406	470	9.0 nM	Hg(II)	CDs	51
GNS/BPA	Reflux, 180 °C, 6 h	300	433	~56 and ~45 nM	Cr(VI) and Hg(II)	f-GNS	This work

the previous reports on the transfer/engagement of electrons[56] of the catalyst f-GNS to the metal d-orbitals, which can be associated with the process of fluorescence. Originally, f-GNS have many flexible binding/active sites (such as –N and –O due to their large chain structure) for interaction with the d-orbital metal ions, as shown in Fig. 6(a). Moreover, the electrons present on the defect sites or active sites of f-GNS were transferred to the d-orbitals of Cr(VI) and Hg(II), which resulted in fluorescence quenching (non-radiative type),[57] as shown in Fig. 6(b). As per our understanding, these BPA-functionalized f-GNS have a very complex structure with the flexibility of the electron donor moieties of the BPA chain present on the f-GNS surface towards Cr(VI) and Hg(II) ions and would require intensive studies to optimize the entire process in detail, which would be a topic for further research.

3.7 Cytotoxicity assay

A cytotoxicity assay carried out for f-GNS against *E. coli*[58] (ATCC 25922) was evaluated using optical density measurements. In Fig. 7(a and b), the effect of different dosages of f-GNS on the growth of *E. coli* can be observed *via* agar diffusion and quantitative evaluation methods. The cytotoxicity examination

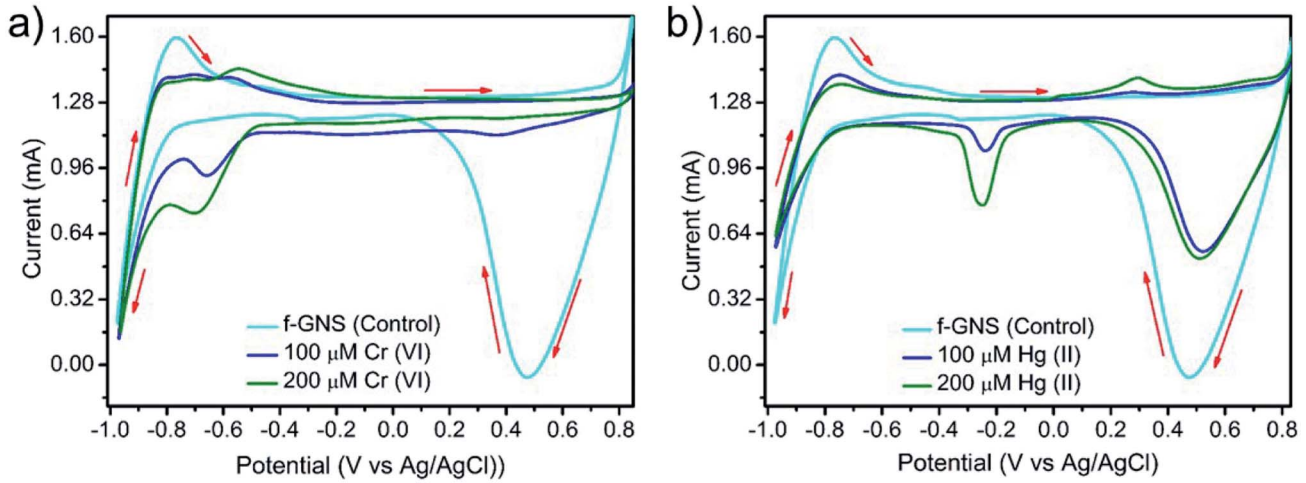

Fig. 5 The cyclic voltammograms for the electrochemical sensing of the metal ions using a three-electrode system sensing of (a) Cr(VI) and (b) Hg(II) by f-GNS.

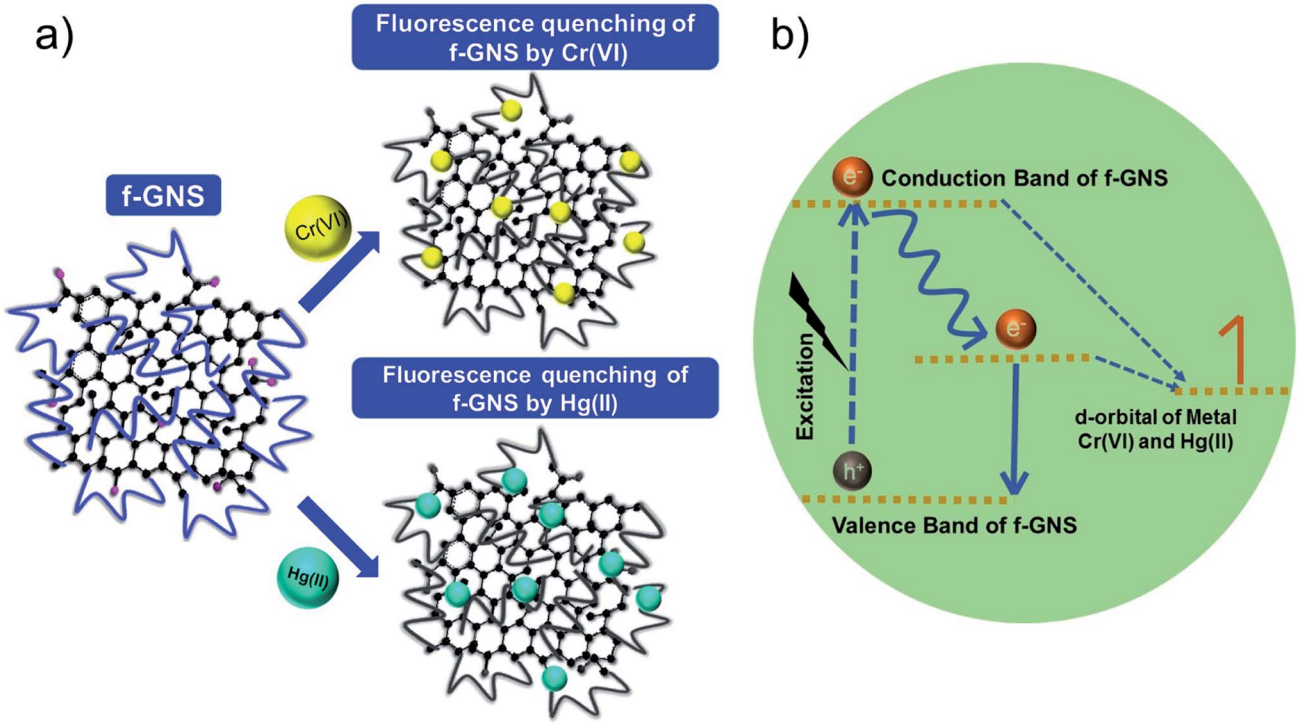

Fig. 6 (a) Schematic diagram showing the fluorescence quenching of f-GNS by Cr(VI) and Hg(II) and (b) a plausible mechanism for the process of fluorescence quenching.

involved the treatment of *E. coli* cultures with different concentrations (5 mg mL^{-1}, 10 mg mL^{-1}, and 15 mg mL^{-1} including the control sample (0 mg mL^{-1})) of f-GNS, and we did not observe any kind of reduction in the growth of bacteria, as visualized by the agar well diffusion method in Fig. 7(a). This observation can be correlated with Fig. 7(b), in which no reduction is observed in the optical density of the cultures, indicating the non-toxic behavior of f-GNS towards the *E.coli* cells.

3.8 Fluorescent ink application

The blue fluorescence emission of f-GNS was investigated for printing applications. f-GNS were used here as a fluorescent ink,[28] which could be used in document writing, security

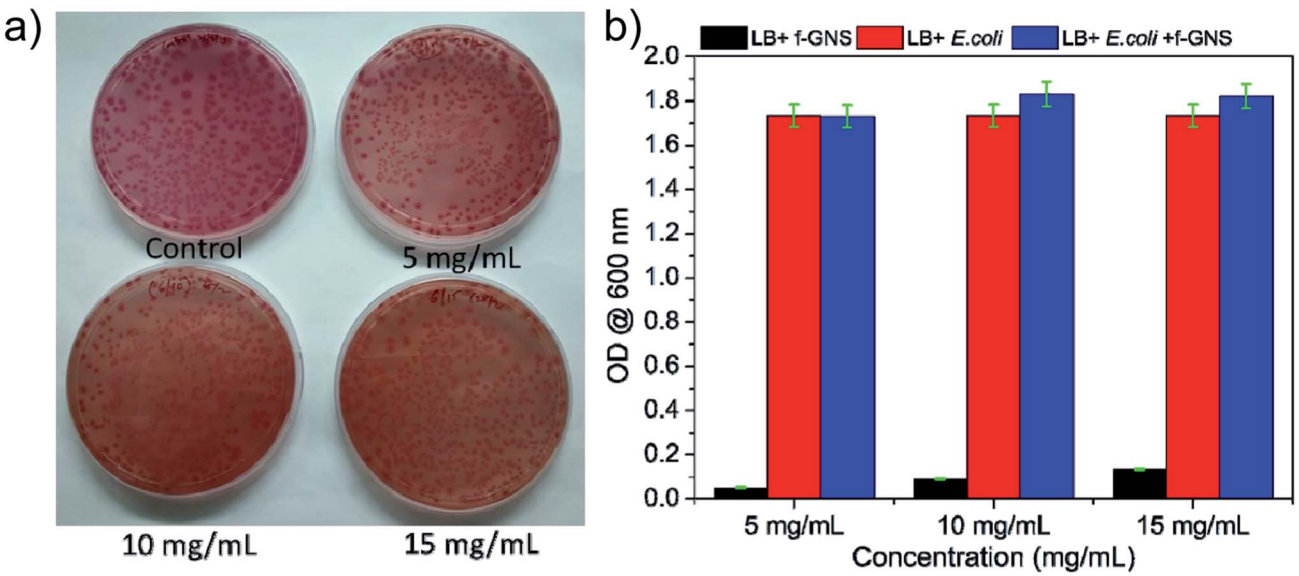

Fig. 7 Effect of different concentrations of f-GNS on *E. coli* growth *via* (a) agar diffusion method and (b) quantitative evaluation method showing the non-toxic behavior of f-GNS.

Fig. 8 Fluorescent ink used on the cartoon flower stamp: (a) under normal daylight and (b) on exposure to UV-visible light, showing blue emission.

features, printing, stamps, *etc.* Fig. 8(a) shows the cartoon flower stamps printed on a TLC paper observed under normal daylight compared to Fig. 8(b), which shows imprinted bright blue fluorescent cartoon flower stamps when observed under UV-visible light illumination.

4. Conclusion

The present work demonstrated a simple methodology for the synthesis of non-toxic blue fluorescent f-GNS *via* surface functionalization using an amine block polymer. On surface functionalization, f-GNS showed practicality in different fields. The excellent photostability, sensitivity, and selectivity of f-GNS were useful in the selective sensing of toxic Cr(VI) and Hg(II) in aqueous media. As well, f-GNS were proven to be biocompatible, which made them promising sensing materials for use as carriers, especially for drug delivery. Moreover, f-GNS were explored as a fluorescent ink on a TLC paper. Nevertheless, the mechanism of the selective sensing of metal ions is still unclear and needs to be understood in detail.

Conflicts of interest

There are no conflict to declare.

Acknowledgements

R. A. thanks MNIT Jaipur for doctoral fellowship, S. R. A. thanks DST, New Delhi for funding, D. S. thanks DST Inspire for doctoral fellowship, G. thanks CSIR for senior research fellowship, and S. K. S. thanks DST (SB/EMEQ-383/2014) and CSIR (01(2854)/16/EMR-II) for funding. S. K. S. thanks Dr Shyam Chaudhary from Tata Steel for providing the graphene samples. S. K. S. thanks Material Research Centre (MRC), MNIT Jaipur for material characterization.

References

1 L. Cao, M. J. Meziani, S. Sahu and Y.-P. Sun, *Acc. Chem. Res.*, 2013, **46**, 171–180.
2 K. M. Tripathi, A. K. Sonker, A. Bhati, J. Bhuyan, A. Singh, A. Singh, S. Sarkar and S. K. Sonkar, *New J. Chem.*, 2016, **40**, 1571–1579.
3 K. M. Tripathi, A. Singh, A. Bhati, S. Sarkar and S. K. Sonkar, *ACS Sustain. Chem. Eng.*, 2016, **4**, 6399–6408.
4 P. G. Luo, S. Sahu, S.-T. Yang, S. K. Sonkar, J. Wang, H. Wang, G. E. LeCroy, L. Cao and Y.-P. Sun, *J. Mater. Chem. B*, 2013, **1**, 2116–2127.
5 K. M. Tripathi, A. Bhati, A. Singh, N. R. Gupta, S. Verma, S. Sarkar and S. K. Sonkar, *RSC Adv.*, 2016, **6**, 37319–37329.
6 T. G. Ros, A. J. van Dillen, J. W. Geus and D. C. Koningsberger, *Chem.–Eur. J.*, 2002, **8**, 1151–1162.
7 P. Dubey, K. M. Tripathi, R. Mishra, A. Bhati, A. Singh and S. K. Sonkar, *RSC Adv.*, 2015, **5**, 87528–87534.
8 P. G. Luo, F. Yang, S.-T. Yang, S. K. Sonkar, L. Yang, J. J. Broglie, Y. Liu and Y.-P. Sun, *RSC Adv.*, 2014, **4**, 10791–10807.
9 C.-T. Hsieh, D.-Y. Tzou, K.-Y. Hsieh and K.-M. Yin, *RSC Adv.*, 2017, **7**, 18340–18346.
10 X. Zhong, J. Jin, S. Li, Z. Niu, W. Hu, R. Li and J. Ma, *Chem. Commun.*, 2010, **46**, 7340–7342.
11 M. Quintana, K. Spyrou, M. Grzelczak, W. R. Browne, P. Rudolf and M. Prato, *ACS Nano*, 2010, **4**, 3527–3533.
12 Z. Sun, D. Guo, S. Wang, C. Wang, Y. Yu, D. Ma, R. Zheng and P. Yan, *RSC Adv.*, 2016, **6**, 65422–65425.
13 H. He and C. Gao, *Chem. Mater.*, 2010, **22**, 5054–5064.
14 N. Mohanty and V. Berry, *Nano Lett.*, 2008, **8**, 4469–4476.
15 Z. Liu, J. T. Robinson, X. Sun and H. Dai, *J. Am. Chem. Soc.*, 2008, **130**, 10876–10877.
16 H. Chen, M. B. Müller, K. J. Gilmore, G. G. Wallace and D. Li, *Adv. Mater.*, 2008, **20**, 3557–3561.
17 X. Zuo, S. He, D. Li, C. Peng, Q. Huang, S. Song and C. Fan, *Langmuir*, 2010, **26**(3), 1936–1939.
18 M. A. Omole, I. O. K'Owino and O. A. Sadik, *Appl. Catal., B*, 2007, **76**, 158–167.
19 A. Bhati, S. R. Anand, D. Saini, Gunture and S. K. Sonkar, *npj Clean Water*, 2019, **2**, 12.
20 Y. Yang, G. Wang, Q. Deng, D. H. L. Ng and H. Zhao, *ACS Appl. Mater. Interfaces*, 2014, **6**, 3008–3015.
21 H. Abdullah and D.-H. Kuo, *ACS Appl. Mater. Interfaces*, 2015, **7**, 26941–26951.
22 V. V. Kumar and S. P. Anthony, *Sens. Actuators, B*, 2016, **225**, 413–419.
23 L.-N. Liu, L. He, Y. Qu, N. Lu, Q.-Y. Cao and Z. Yan, *Inorg. Chim. Acta*, 2018, **474**, 128–133.
24 V. Velma, S. S. Vutukuru and P. B. Tchounwou, *Rev. Environ. Health*, 2009, **24**, 129–145.
25 K. Daware, R. Shinde, R. S. Kalubarme, M. Kasture, A. Pandey, C. Terashima and S. W. Gosavi, *Sens. Actuators, B*, 2018, **265**, 547–555.
26 A. Bhati, S. R. Anand, D. Saini, P. Khare, P. Dubey and S. K. Sonkar, *New J. Chem.*, 2018, **42**, 19548–19556.

27 C. Wurth, M. Grabolle, J. Pauli, M. Spieles and U. Resch-Genger, *Nat. Protoc.*, 2013, **8**, 1535–1550.
28 S. R. Anand, A. Bhati, D. Saini, Gunture, N. Chauhan, P. Khare and S. K. Sonkar, *ACS Omega*, 2019, **4**, 1581–1591.
29 P. Khare, A. Singh, S. Verma, A. Bhati, A. K. Sonker, K. M. Tripathi and S. K. Sonkar, *ACS Sustain. Chem. Eng.*, 2018, **6**, 579–589.
30 A. Bhati, A. Singh, K. M. Tripathi and S. K. Sonkar, *Int. J. Photoenergy*, 2016, **2016**, 8.
31 L. Qu, Y. Lin, D. E. Hill, B. Zhou, W. Wang, X. Sun, A. Kitaygorodskiy, M. Suarez, J. W. Connell, L. F. Allard and Y.-P. Sun, *Macromolecules*, 2004, **37**, 6055–6060.
32 G. E. LeCroy, S. K. Sonkar, F. Yang, L. M. Veca, P. Wang, K. N. Tackett, J.-J. Yu, E. Vasile, H. Qian, Y. Liu, P. Luo and Y.-P. Sun, *ACS Nano*, 2014, **8**, 4522–4529.
33 P. Dubey, K. M. Tripathi and S. K. Sonkar, *RSC Adv.*, 2014, **4**, 5838–5844.
34 Z. Li, H. Yu, T. Bian, Y. Zhao, C. Zhou, L. Shang, Y. Liu, L.-Z. Wu, C.-H. Tung and T. Zhang, *J. Mater. Chem. C*, 2015, **3**, 1922–1928.
35 J. N. Wang, Q. Qi, L. Zhang and S. H. Li, *Inorg. Chem.*, 2012, **51**, 13103–13107.
36 L. Zhang, C. Xu and B. Li, *Microchim. Acta*, 2009, **166**, 61–68.
37 A. Chatterjee, M. Banerjee, D. G. Khandare, R. U. Gawas, S. C. Mascarenhas, A. Ganguly, R. Gupta and H. Joshi, *Am. J. Anal. Chem.*, 2017, **89**, 12698–12704.
38 M. Rong, L. Lin, X. Song, Y. Wang, Y. Zhong, J. Yan, Y. Feng, X. Zeng and X. Chen, *Biosens. Bioelectron.*, 2015, **68**, 210–217.
39 Y. Zhang, X. Fang, H. Zhao and Z. Li, *Talanta*, 2018, **181**, 318–325.
40 Z. Li, Y. Wang, Y. Ni and S. Kokot, *Sens. Actuators, B*, 2015, **207**, 490–497.
41 D. Dinda, B. K. Shaw and S. K. Saha, *ACS Appl. Mater. Interfaces*, 2015, **7**, 14743–14749.
42 H. Guo, J. Li, Y. Li, D. Wu, H. Ma, Q. Wei and B. Du, *New J. Chem.*, 2018, **42**, 11147–11152.
43 Y. W. He, Y. Feng, L. W. Kang and X. L. Li, *J. Chem.*, 2017, **2017**, 1–5.
44 L. Wang, T. Yao, S. Shi, Y. Cao and W. Sun, *Sci. Rep.*, 2014, **4**, 5320.
45 P. Li, Y. Hong, H. Feng and S. F. Y. Li, *J. Mater. Chem. B*, 2017, **5**, 2979–2988.
46 V. K. Singh, V. Singh, P. K. Yadav, S. Chandra, D. Bano, V. Kumar, B. Koch, M. Talat and S. H. Hasan, *New J. Chem.*, 2018, **42**, 12990–12997.
47 P. M. Carrasco, I. García, L. Yate, R. Tena Zaera, G. Cabañero, H. J. Grande and V. Ruiz, *Carbon*, 2016, **109**, 658–665.
48 S. Song, F. Liang, M. Li, F. Du, W. Dong, X. Gong, S. Shuang and C. Dong, *Spectrochim. Acta, Part A*, 2019, **215**, 58–68.
49 A. K. Singh, V. K. Singh, M. Singh, P. Singh, S. R. Khadim, U. Singh, B. Koch, S. H. Hasan and R. K. Asthana, *J. Photochem. Photobiol.*, 2019, **376**, 63–72.
50 K. Patir and S. K. Gogoi, *ACS Sustain. Chem. Eng.*, 2018, **6**, 1732–1743.
51 J. Zhao, M. Huang, L. Zhang, M. Zou, D. Chen, Y. Huang and S. Zhao, *Am. J. Anal. Chem.*, 2017, **89**, 8044–8049.
52 C. Shan Lim, K. Hola, A. Ambrosi, R. Zboril and M. Pumera, *Electrochem. Commun.*, 2015, **52**, 75–79.
53 Y. Tian, L. Li, X. Guo, A. Wójtowicz, L. Estevez, M. J. Krysmann and A. Kelarakis, *Chem. Commun.*, 2018, **54**, 9067–9070.
54 R. L. Birke, M.-H. Kim and M. Strassfeld, *Am. J. Anal. Chem.*, 1981, **53**, 852–856.
55 O. Kurtz, J. Barthelmes, R. Ruther, F. Lagorce, M. Ruge and C. Donner, *Study of corrosion protection mechanisms with the help of cyclic voltammetry*, 2012, vol. 103, pp. 1209–1218.
56 H. Huang, L. Liao, X. Xu, M. Zou, F. Liu and N. Li, *Talanta*, 2013, **117**, 152–157.
57 H. Zhang, Y. Chen, M. Liang, L. Xu, S. Qi, H. Chen and X. Chen, *Am. J. Anal. Chem.*, 2014, **86**, 9846–9852.
58 P. Khare, A. Singh, S. Verma, A. Bhati, A. K. Sonker, K. M. Tripathi and S. K. Sonkar, *ACS Sustain. Chem. Eng.*, 2018, **6**(1), 579–589.